Supporting Information:

Circular Dichroism Measurement of Single Metal Nanoparticles Using Photothermal Imaging

Patrick Spaeth,[†] Subhasis Adhikari,[†] Laurent Le,[†] Thomas Jollans,[†] Sergii Pud,[†] Wiebke Albrecht ,[†,‡] Thomas Bauer,[¶] Martín Caldarola,*,[¶,§] L. Kuipers,[¶] and Michel Orrit*,[†]

[†]Huygens–Kamerlingh Onnes Laboratory, Leiden University, 2300 RA Leiden, Netherlands

[‡]EMAT, University of Antwerp, Groenenborgerlaan 171, B-2020 Antwerp, Belgium

[¶]Kavli Institute of Nanoscience Delft, Department of Quantum Nanoscience, Delft University of Technology, Lorentzweg 1, 2628 CJ Delft, The Netherlands

[§]Kavli Institute of Nanoscience Delft, Department of Bionanoscience, Delft University of Technology, Lorentzweg 1, 2628 CJ Delft, The Netherlands

E-mail: m.caldarola@tudelft.nl; orrit@physics.leidenuniv.nl

Details of the experimental setup

The schematic of our photothermal circular dichroism setup is shown in Figure 2 in the main text. Here, we explain all the components in details. We used a Coherent Verdi laser (Model: V10-A0366, wavelength of 532 nm) as a heating beam which was passed through an electro-optical modulator (EOM) from Qioptiq (Model: LM0202) for modulating between two orthogonal linear polarizations. The modulation frequency was set by a function generator (from Tektronix, Model: AFG3102) which sends the signals to a digital amplifier (from Qioptiq, Model: DIV20) to amplify the signal before sending it to the EOM. The function generator sends the same signal also to the lock-in amplifier (from Stanford Research Systems, Model: SR844) as a reference signal. For Koehler-like illumination a lens with focal length of 50 cm was used to focus the heating beam at the back focal plane of an oil-immersion objective (from Olympus, PLAPON, 60X, NA = 1.45) and to illuminate the back focal plane of the objective with low numerical aperture (NA = 0.025 which corresponds to a diffraction-limited spot of 10 μm diameter). A quarter-wave plate (Thorlabs) was used to convert the linear polarization to circular and thus we modulated the heating beam between left and right circular polarizations to measure photothermal circular dichroism. The polarization state of light was analyzed using a polarization analyzer (Schäfter + Kirchhoff GmbH, model SK010PA-VIS).

A non-polarizing 50/50 beam splitter (Thorlabs) was used to transmit the heating beam and to reflect the probe beam. The collimated probe beam (Ti-Sapphire laser from Spectra-Physics, wavelength 780 nm, Model: 3900S) was focused by the objective in its focal plane. To detect the back-scattered probe beam signal efficiently, we used a "cat-eye reflector" configuration (a combination of polarizing beam splitter (PBS) and quarter-wave plate). The back-scattered probe signal was then filtered out from the heating beam by using a long-pass (750 LP) filter and focused into a photodiode (PD) from Femto (Model: DHPCA-100-F, with an amplification of 10^6) using a lens of focal length 7.5 cm. We note that the reported laser powers both in the main text and SI are measured just before the oil-

immersion objective. The photodiode signal was then sent to the lock-in amplifier as an input signal. A flippable polarizer was used to switch between normal photothermal and photothermal circular dichroism measurements. For normal photothermal microscopy, we inserted a polarizer after the EOM to achieve intensity modulation; for the photothermal circular dichroism, we removed the polarizer to keep the modulation between left and right circular polarizations. To obtain an image, we scan the sample by translating the sample stage using a piezo stage (PI P.611.3.5 Nanocube) while keeping the overlap between the heating and probe beams constant.

Sample design and preparation

We designed a sample that contains an array of alternating structures following the pattern showed in figure S1 (a). We have three types of structures: left-handed (L), right-handed (R) and achiral (A). The individual designs and dimensions of these structures are shown in figure S1 (b); all the structures have a height of 70 nm.

The sample with the array of nanostructures was prepared using e-beam lithography and lift-off. First, glass coverslides were cleaned by sonication in acetone and then in isopropanol for 5 minutes each. Next, the coverslides were coated with PMMA e-beam resist in the following steps: 1) Dehydration of the glass slide surface by baking on a hot plate at 180°C for 5 minutes, 2) Spin coating PMMA 950K, dilution 6% in anisole at 4000 rpm, which results in 300 nm layer thickness, 3) Baking the glass slide for 5 min at 180 °C. After spin-coating, the samples were coated with 15 nm of Cr using a Temescal FC-2000 e-beam evaporator. This sacrificial layer of Cr serves to prevent charging effects on the glass during e-beam patterning. The pattern was written using e-beam (Raith EBPG 5000+) with a beam step size of 1 nm
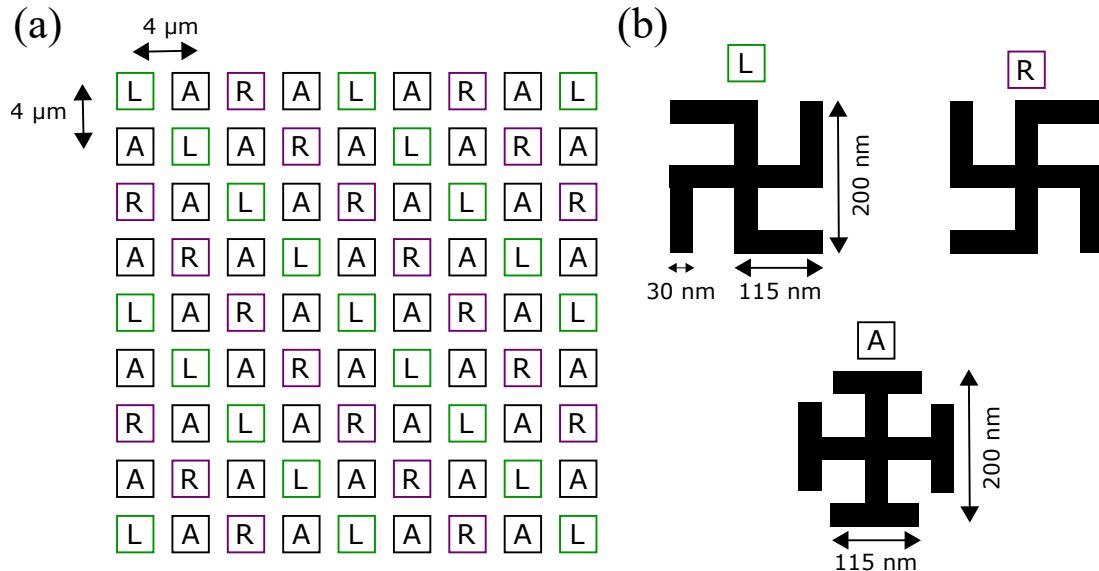

Figure S1: **Design of the checkerboard sample**. (a) Array design, showing the alternation of the three types of structure: left-handed (L), right-handed (R) and achiral (A). (b) Detail of the design of each type of structure. The height of the structures is 70 nm.

and a dose of $2000\,\mu\mathrm{C\ cm^{-2}}$, which was found to be optimal through a dose test. Following the exposure, the Cr layer was stripped by wet etching in a TechniEtch Cr01 (MicroChem) for 25 s and the sample was rinsed with deionized water. The pattern was developed by submerging the sample for 1 minute in a mixture of MIBK (methylisobutylketone) and IPA (isopropanol) (1:3 v/v) and further submerging into IPA for 1 minute. Finally, 70 nm of gold was evaporated onto the sample using a Temescal FC-2000 and followed by a lift-off procedure (10 minutes in n-methylpyrrolidone at $80\,^{\circ}\mathrm{C}$). The sample was then rinsed with acetone and IPA and spin-dried at 2000 rpm.

After nanofabrication we prepared the sample for the optical measurements. We sandwiched the sample with a second cavity glass slide (Menzel #1.5) to provide space for a liquid. We chose toluene as a liquid medium because it provides a high thermorefractive coefficient ($\partial n/\partial T = -5.68 \times 10^{-4}\ \mathrm{K^{-1}}$) which is essential for PT imaging[S1].

After optical imaging, the sample was sputtered with 5 nm of platinum to make it conductive for proper imaging under a scanning electron microscope (SEM). SEM images are shown in Figure 4 in the main text.

Numerical simulations

We performed numerical simulations to calculate the absorbed power for right and left circularly polarized light by the idealized gammadia structures on a glass substrate embedded
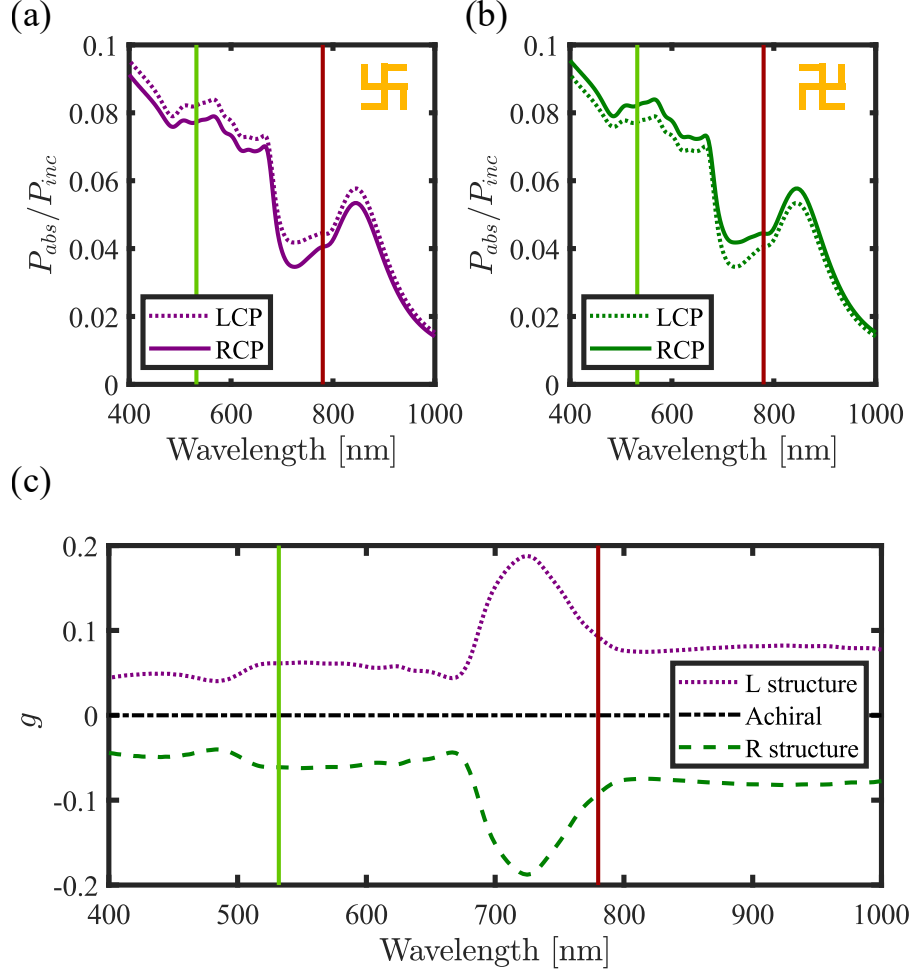

Figure S2: **Absorption and g factor numerical results for ideal gammadia**. (a) Normalized absorbed power for a single left-handed gammadion structure (shown in the inset) on a glass substrate embedded in toluene. Note that the structure is now seen from the glass side and corresponds to the definition of Figure 3 as left-handed. The absorption for LCP is higher than for RCP. (b) Normalized absorbed power for the right-handed gammadion structure (shown in the inset) on a glass substrate embedded in toluene. For this right-handed structure, the absorption for RCP is higher than for LCP. (c) Dissymmetry factor g as defined in equation 2 in the main text for both structures. Additionally we show the achiral structure, showing null chirality, as expected from symmetry arguments. The vertical lines in the plots correspond to the heating wavelength, $532\,\mathrm{nm}$ (in green), and the probe wavelength, $780\,\mathrm{nm}$ (in red). The absolute value of g at the heating wavelength is ~ 0.061.

in toluene. The dimensions used for the simulations are the ones depicted in figure S1 on the right, with a height of 70 nm. We used the commercial FDTD software Lumerical with a total-field scattered-field source[S2] to simulate the plane wave heating laser and we calculated the absorbed power by the structures as

$$P_{abs} = -\frac{1}{2}\omega|\mathbf{E}|^2\Im(\epsilon)\,, \tag{1}$$

where ω is the frequency of the incoming wave, $\mathbf{E}$ is the electric field in the structure and $\Im(\epsilon)$ represents the imaginary part of the permittivity[S3]. Note that this is calculated for every voxel in the simulation and then integrated over an $800\,\text{nm}\times800\,\text{nm}\times800\,\text{nm}$ volume to calculate the total absorbed power for each illumination condition. We also calculated the absorption cross section of the gammadia at 532 nm, obtaining 2.2×10^4 nm^2.

In the simulation, we place the R or L gammadia made of gold on a glass substrate. For the gold structure we took the dielectric function built in the software (Gold (Au) - CRC)[S4] and the one of glass from Palik[S5]. The refractive index of toluene was taken from the work by Kedenburg et. al.[S6].

We excite the structure with a plane wave coming from the substrate side, using left and right circularly polarized light (equivalently to what we do experimentally) and for each case we calculate the absorbed power normalized by the incident power P_{abs}/P_{inc}. Figure S2 (a) shows the obtained spectra for both circular polarization states for the left-handed structure and Figure S2 (b) for the right-handed structure. Note that the former absorbs more when excited with LCP and the opposite situation holds for the latter. The inset depicts the schematics of both structures seen from the top (as is seen in a SEM image). The vertical lines show the locations of the heating beam (green) and the probe beam (red), for reference. We note that the absorption for the probe beam is not negligible. Thus, we kept the probe power low for our measurements.

Figure S2 (c) shows the dissymmetry factor spectra $g(\lambda)$ for both structures. Naturally, they only differ in the sign, being positive for the L structure and negative for the R structure

in the studied range. For completeness we also simulated the achiral ideal structures, that exhibit null dissymmetry factor. Note that the calculated value for the dissymmetry at the heating wavelength is $g \sim 0.061$.

We also checked that the g factor values flip sign when we repeat the simulation with an exciting wave coming from the solvent side (we changed the wavevector from $\mathbf{k} \propto +\hat{\mathbf{z}}$ to $\mathbf{k} \propto -\hat{\mathbf{z}}$). This is the expected behaviour since the gammadia seen from the opposite side will have the opposite handedness.

Supplementary videos

We also provide movies depicting results from the simulations, for the case of a right-handed gammadion, illuminated with right and left circularly polarized light.

The Movie S1 depicts two intensity maps for the right-handed structure, with left (on the left side) and right (on the right side) CPL illumination at a single wavelength, $\lambda = 532\,\text{nm}$. Time evolves from zero to $t_f = \lambda 4\pi/c$, where c is the speed of light in vacuum, so the full video corresponds to 2 complete optical cycles. As can be seen, the absence of time-reversal symmetry supports the difference in absorption for the two polarizations in a direct, visual way. To further show this in a pictorial way, we performed the difference of these two maps and prepared the Movie S2 depicting the time evolution of the difference $I_{LCP}(t) - I_{RCP}(-t)$.

Measurement of linear dichroism on gammadia

Linear dichroism is defined as the differential absorption between two orthogonal linear polarizations states:

$$LD_{\hat{\mathbf{n}}} = \sigma_{\parallel} - \sigma_{\perp}, \tag{2}$$

where $\sigma_{\parallel}$ and $\sigma_{\perp}$ represent the absorption cross section for a polarization state parallel and perpendicular to a direction given by the vector $\hat{\mathbf{n}}$, respectively.
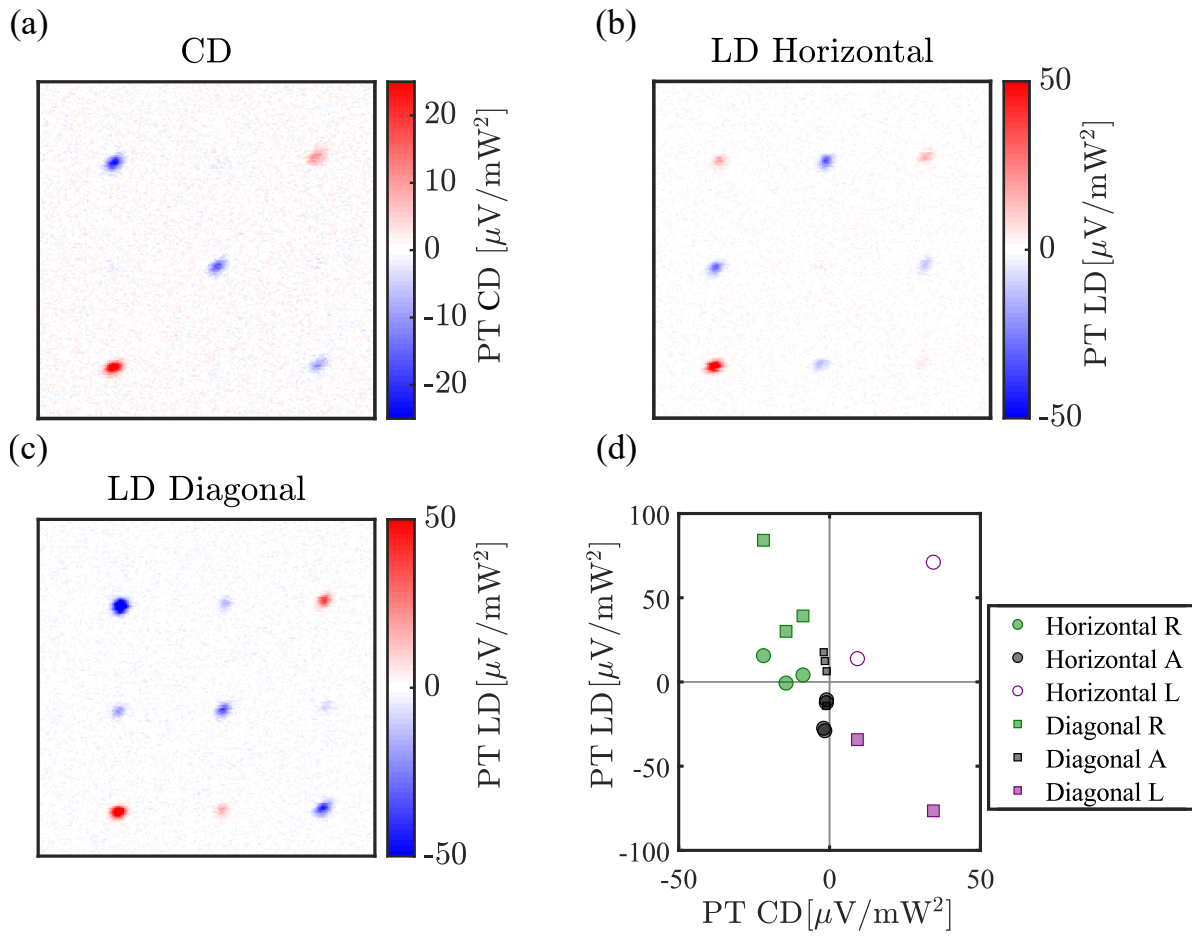

Figure S3: **Linear dichroism measurements of the gammadion sample**. (a) Photothermal circular dichroism image of 9 gammadia (the same as shown in figure 4 (b) and (d) in the main text). (b) Photothermal linear dichroism image of the same area as (a), with horizontal-vertical modulation (90° and 0°). (c) Photothermal linear dichroism in the diagonal direction, i.e. polarization modulation between 45° and −45°. (d) Correlation plot of the PT CD and PT LD.

We performed different measurements of photothermal LD in the horizontal direction, by modulating the incoming polarization state of the heating beam between linear horizontal and vertical polarization states. To achieve this we removed the quarter-wave plate from the setup. We also measured with respect to the diagonal state (rotated 45°), obtained by adding a half-wave plate. The reason for doing these two types of polarization modulation is to obtain full information about the linear dichroism signals.

Figure S3 shows the photothermal LD images of the same gammadia structures as shown in Figure 3(b) in the main text. We clearly see non-zero linear dichroism signals, of similar order but stronger than circular dichroism signals. We attribute this to the fabrication imperfections in the sample, which break the symmetry of the structures. As figure S3 (d) shows, there is no obvious correlation between LD and CD.

Characterization of nanospheres shape and size

We studied in detail the morphological characteristics of the nanospheres used for the optical imaging by performing High-Angle Annular Dark-Field Scanning Transmission Electron Microscope (HAADF-STEM) imaging on a dispersion of such nanoparticles. The HAADF-STEM images were acquired using a Thermo Fisher Scientific Tecnai Osiris microscope operated at 200 kV with a 50 pA beam current and a frame time of 6 s. All tomography series were acquired by taking projection images over an angular range of $\pm 75°$ with a tilt increment of 3° with a frame time of 6 s. After alignment of the projection images by using a cross correlation, the stacks of aligned projection images served as inputs for 20 iterations of the expectation maximization reconstruction implemented in the ASTRA toolbox[S7].

Figure S4 shows representative HAADF-STEM images of gold nanospheres from the same synthesis batch at different resolutions. In figure S4 (a) we present a zoom on the remarkably non-spherical particles, marked with an arrow. In figure S4 (b) we zoom in further and again present in the rectangles a closer image of a few non-spherical particles. Figures S4 (c) and (d) depict higher resolution images where the facets of some of the nanoparticles imaged can be clearly appreciated. The arrows point to the non-spherical shaped nanoparticles we found. In addition, the arrow in figure S4 (d) shows a particle with defect in the crystalline structure.

From the 2D images it can be observed that most nanospheres are isotropic. However, some nanospheres display lattice defects or are anisotropic. The defects are most likely twin boundaries as evident from the contrast difference in the HAADF-STEM images for such particles. Because the displayed images are only 2D projections of the real 3D object, we also performed electron tomography to obtain the 3D shape of a characteristic nanosphere. The visualization of the tomography reconstruction for a characteristic particle as well as orthoslices through the reconstruction are added in the supplementary Movie S3.

In addition, we quantified the size distribution of our sample of nanoparticles by extracting the measured diameter from STEM images. The obtained histogram is depicted in figure
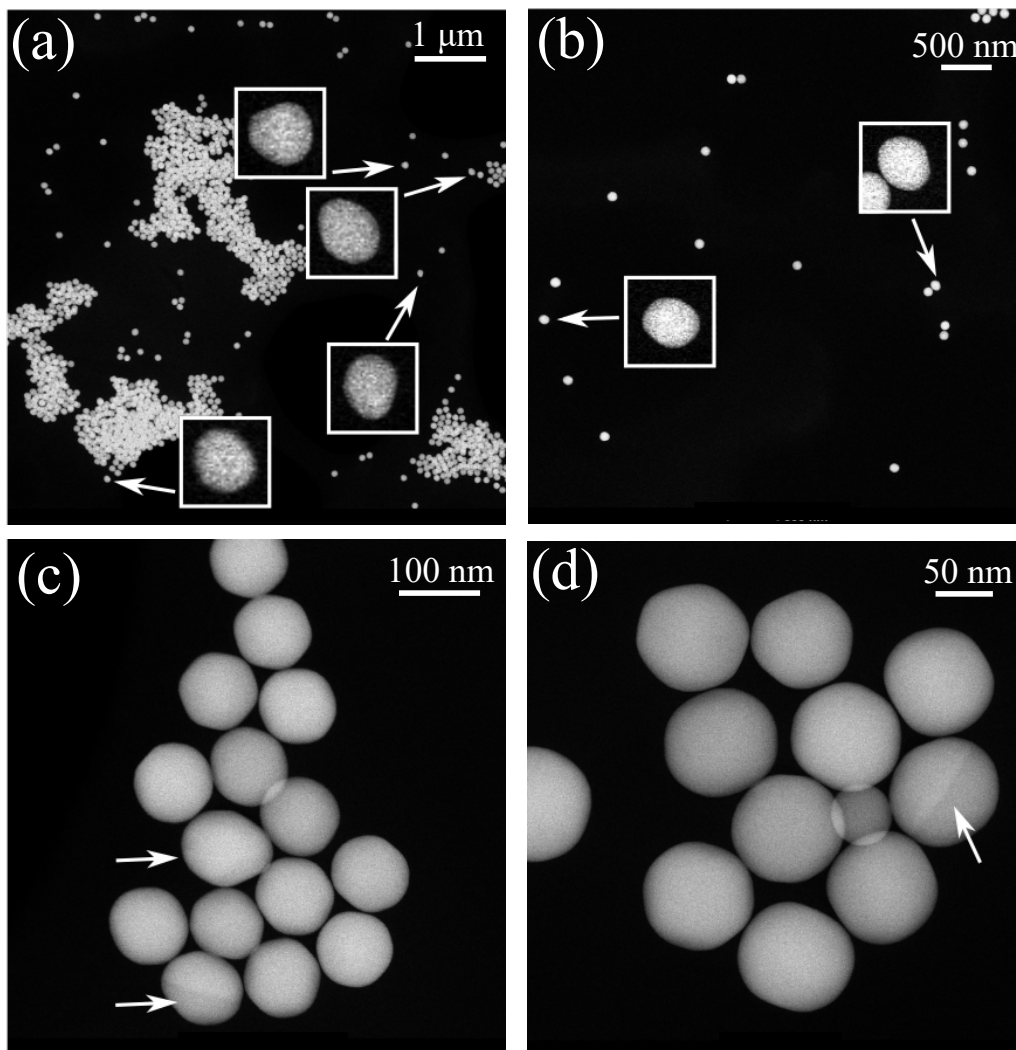
Figure S4: **HAADF-STEM images of gold nanospheres**. (a) Large area scan to provide an overview of many nanoparticles. The rectangles contain a zoomed image on the particles marked with arrows, where non-spherical shape is clearly observed. (b) Image of a different area of the sample, with higher magnification than in (a). Again, we show in the rectangles a zoom on the particles marked with arrows. (c) Higher resolution image of a cluster of nanoparticles. The arrows depict the particles with the strongest deviation from spherical shape. (d) Closer look on another cluster of particles, where the arrow now depicts a particle with defects in the crystalline structure. Most particles exhibit faceted spherical-like shapes. However, a fraction of the nanospheres are anisotropic and/or exhibit crystal defects as evident from the contrast difference. Examples of such particles are marked by arrows in the images. The scale bars are shown in each panel.

S5. While the nominal diameter given by the manufacturer (Nanocomposix) is 100 nm we measured an average value of 94 nm.
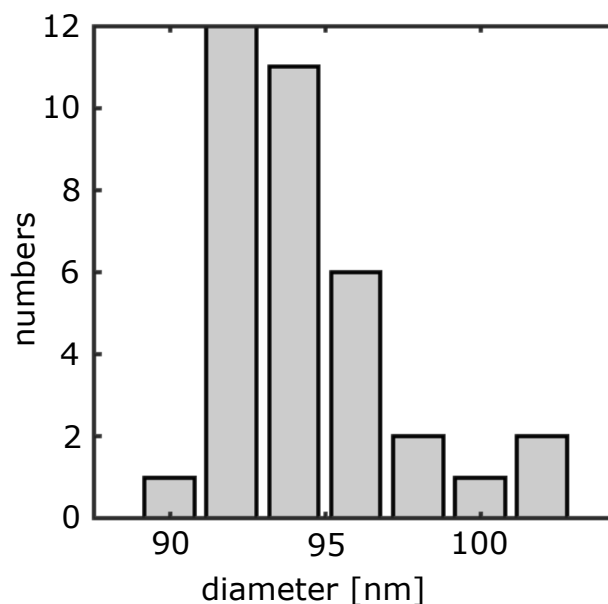
Figure S5: **Size distribution of the nanoparticles from HAADF-STEM**. The particle sizes are calculated from 35 single particles from the images shown in Figure S4 (b). The average particle size is 94 nm with a size dispersion of 3%.

Does linear dichroism influence photothermal circular dichroism?

In order to characterize the crosstalk in our photothermal circular dichroism signal with linear dichroism, we measured both circular dichroism and linear dichroism of the same nanoparticles that were characterized in the previous section.

Figure S6 shows photothermal, photothermal circular dichroism and photothermal linear dichroism signals of single 100 nm gold nanospheres. The value of the nanosphere size is 100 nm as provided by the manufacturer, however the average particle size calculated from STEM image is nearer 94 nm (see Figure S5). Note that the colour scale in photothermal circular dichroism and photothermal linear dichroism images are 100 times and 10 times smaller than PT image, respectively. Most particles show weak circular dichroism but strong linear dichroism signal. This indicates that there is little crosstalk between the photothermal circular dichroism signal and linear dichroism. We attribute the linear dichroism signal of

nanospheres to shape and crystallinity imperfections of individual nanoparticles.

All the images of PT CD and PT LD of gammadia and gold nanospheres in the main text and in SI are X channel signals of lock in to show phase information. We choose X channel signal instead of Y channel because at our measurement modulation frequency, most nanostructures or nanoparticles show in-phase signals.
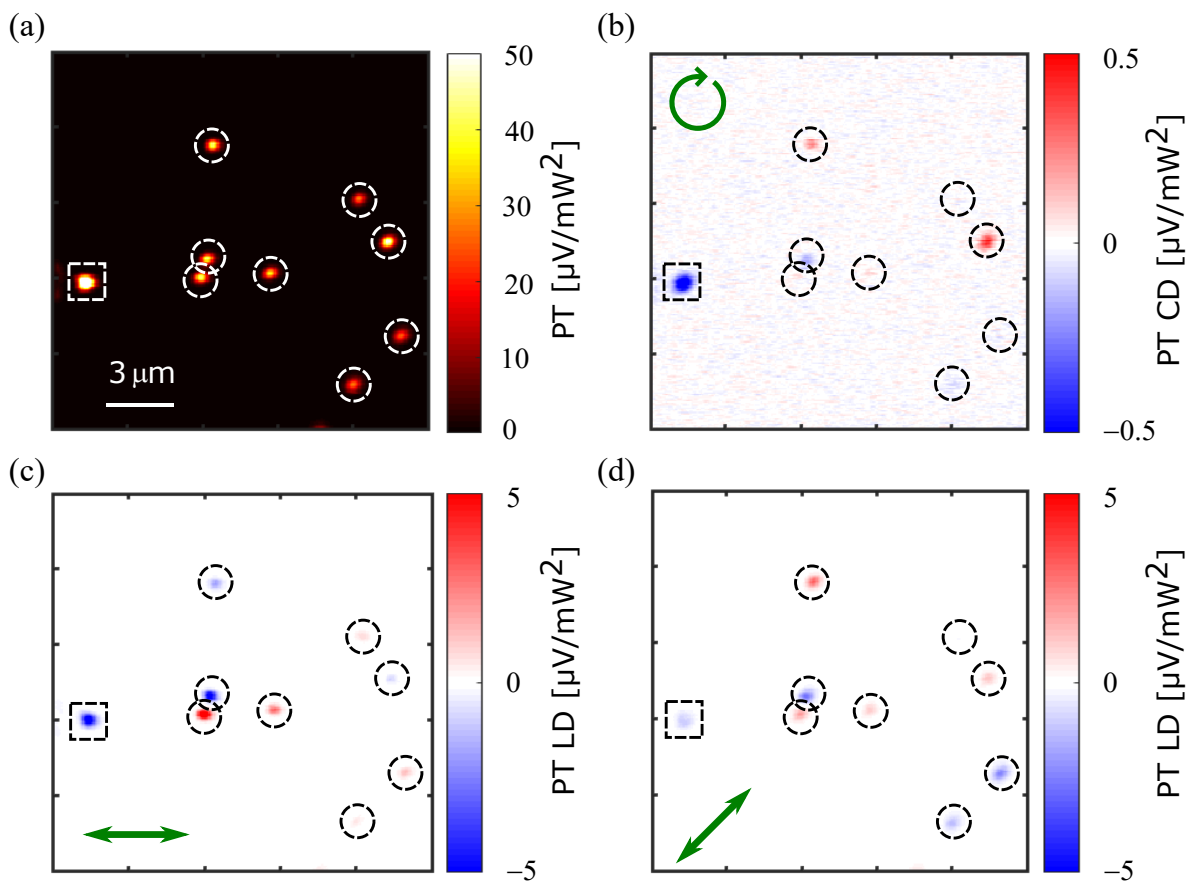

Figure S6: **Circular dichroism and linear dichroism measurements of gold nanospheres**. (a) Photothermal (PT), (b) photothermal circular dichroism (PT CD), (c) photothermal linear dichroism (PT LD) with 90° and 0° (horizontal-vertical) polarization modulation and (d) photothermal linear dichroism (PT LD) with −45° and 45° (diagonals) polarization modulation. Dashed circles are drawn to show single particle spots. The leftmost particle is probably an aggregate and marked with a dashed square box. The arrows show the direction $\hat{\mathbf{n}}$ for the LD.

More measurements of circular dichroism of gold nanospheres

We measured photothermal (PT) and photothermal circular dichroism (PT CD) of single 100 nm gold nanospheres deposited on a glass substrate. The images for two different areas in both imaging modes are shown in Figure S7. Most particles show weak photothermal circular dichroism signals and are distributed between positive and negative PT CD signals.
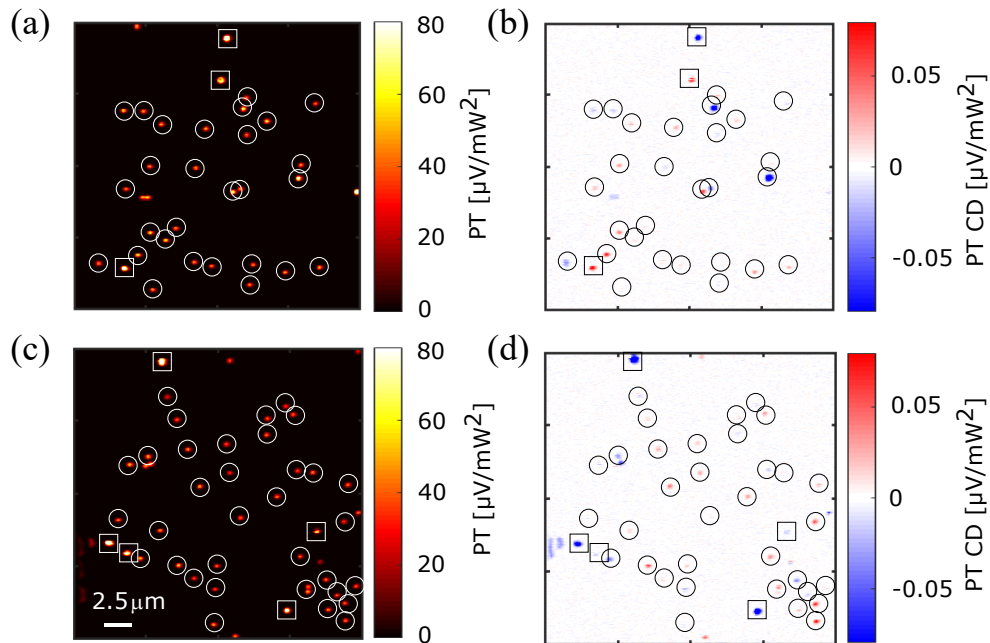

Figure S7: **Circular dichroism measurements of gold nanospheres on glass**. (a) Photothermal (PT) image of an area showing many nanospheres. Note the small dispersion in PT intensities, showing a remarkably small dispersion in size for the nanoparticles. (b) Photothermal circular dichroism (PT CD) of the same area as (a). (c) Photothermal (PT) image of a different area of the sample, showing more nanospheres. (d) Photothermal circular dichroism (PT CD) of the same area as (c). The solid circles are drawn to show correlative image spots between PT and PT CD images and to show which particles are considered for the correlation and histogram analyses. Extremely bright particles (marked with solid square boxes) in the photothermal image are probably aggregates and were ignored for the analysis. We also ignored the particles which are on the edge of the scan for the analysis.

We calculated the g factor by averaging the signal of 3×3 pixels at the maximum intensity for each spot in the images, excluding exceptionally bright spots in both photothermal and photothermal circular dichroism images, which are assigned to clusters of nanoparticles.

We used equation 2 in the main text for the g factor definition. A correlation plot of g factor and photothermal signal of 59 single gold nanospheres is shown in Figure S8 along with corresponding histogram of g factors. Most particles show g factors less than 1% and normally distributed between positive and negative signals, with a small mean value of 0.16% (which may be the experimental bias).
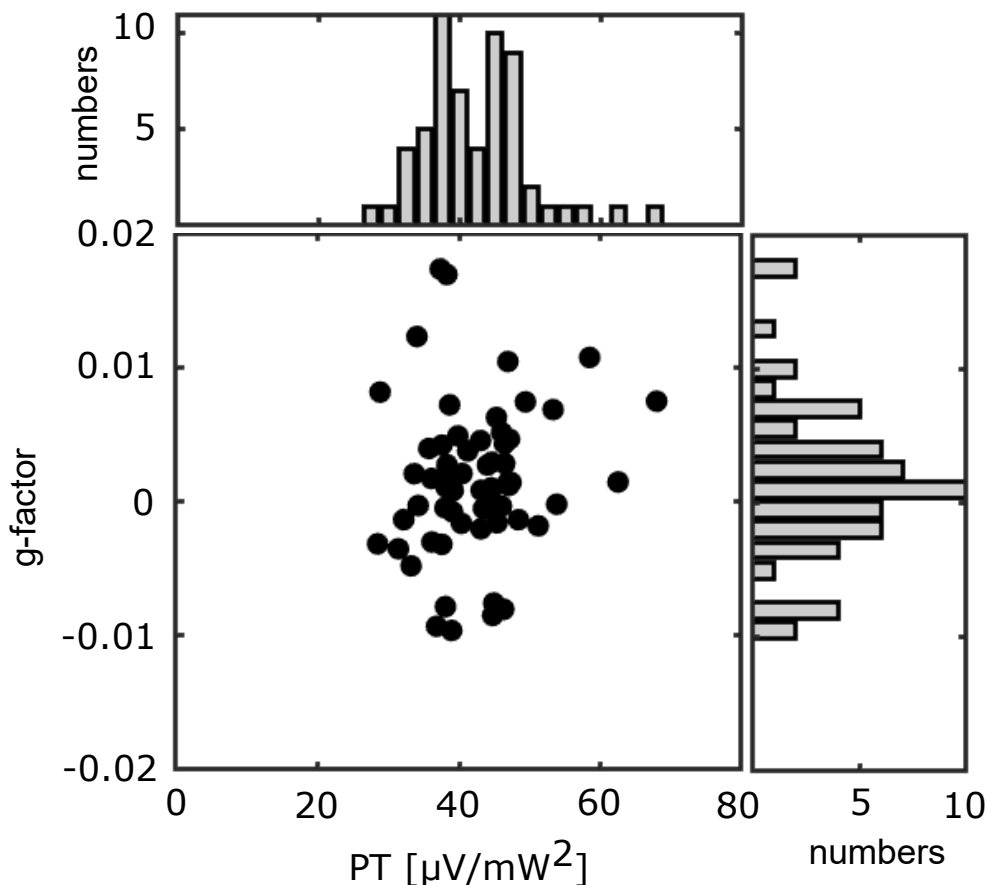

Figure S8: **Histogram of PT and PT CD of gold nanospheres on glass**. Correlation plot of measured g factor and photothermal signal and histograms of photothermal signal and g factor. The histogram of photothermal signal looks narrow, which is consistent with the histogram of particle sizes shown in Figure S5. The dispersion in particle size is 3% and the dispersion in photothermal signal is 18%. The distribution of photothermal signals follows from the distribution of particle sizes, and from the dispersion in orientations and shapes of the nanoparticles (as we see in Figure S4). Most particles show g factors less than 1%. The mean value of g factor is 0.0016.

For a perfect spherical particle, photothermal circular dichroism is expected to be null. However, a fraction of particles in our measurements are non-spherical in shape and have

defects in their crystal structure as we see from the STEM images in Figure S4. We therefore attribute the observed photothermal circular dichroism signal to the particle's shape and defects. To understand in detail how the particle shape and defects play role in the photothermal circular dichroism signal, a careful correlated optical and TEM-tomography should be performed, which is outside the scope of this work.

Line profiles of PT and PT CD signal of gold nanospheres

To further characterize our PT-CD microscope, we present here representative cross sections from our optical images when the object imaged is smaller than the diffraction limit, i.e. we show a linear profile of the point-spread-function (PSF) of our microscope.

The line profiles of PT and PT CD signals of two gold nanospheres are shown in Figure S9. The point-spread functions of both PT and PT CD signal look similar except for some wrinkles appearing as side bands in PT CD profile. These wrinkles are attributed to low signal-to-noise ratio in PT CD signal.
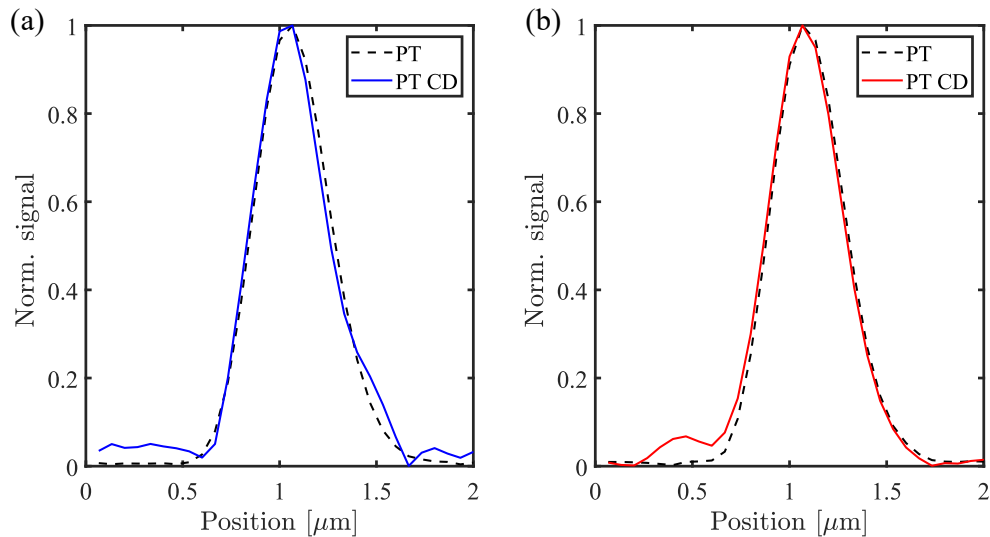
Figure S9: **Line profiles of PT and PT CD of gold nanospheres**. (a) Normalized line profiles of the particle located at the top left in Figure 6(a) and (b) for the intensity-modulated photothermal (PT, black dashed line) and photothermal circular dichroism (blue solid line). (b) Normalized line profiles of the particle located at the top right in Figure 6(a) and (b) for the intensity-modulated photothermal (PT, black dashed line) and photothermal circular dichroism (red solid line). We use color from the colormap in figure 6 (b) to indicate the signal sign and for the particle with negative PT CD signal, the line profile is shown with absolute values. All line profiles are normalized by the maximum peak signals.

Temperature increase due to absorption of the heating and probe beams

The (local) increase in temperature of a nanostructure due to light absorption in the steady state case for a sphere can be calculated as

$$\Delta T = \frac{P_{disp}}{4\pi\kappa R}, \tag{3}$$

where P_{disp} is the power dissipated by the nanosphere, κ is the average thermal conductivity of the medium and the glass substrate ($\kappa = (\kappa_{medium} + \kappa_{glass})/2$) and R is the radius of the nanosphere[S8]. With our experimental parameters, we obtained ΔT_{sphere} of 8 K and 16 K at the heating and probe powers, respectively.

When the structure is not spherical in shape, as it is for our gammadia, there is no simple expression to calculate the temperature increase. However, a common approach for other nanostructure shapes is to use equation 3 replacing the radius R with a fictitious radius R_L that can be calculated for different geometries[S8]. Thus, we used $R_L = 85$ nm in this equation to approximate the increase in temperature, obtaining 11.7 K and 97.5 K at the heating and probe powers, respectively. The boiling temperature of toluene (393 K, or 120 °C, taking surface tension into account) provides an upper bound for the maximum temperature reached by the gammadion.

References

(S1) Gaiduk, A.; Ruijgrok, P. V.; Yorulmaz, M.; Orrit, M. Detection limits in photothermal microscopy. *Chemical Science* **2010**, *1*, 343.

(S2) Lumerical: Sources - TFSF. `https://kb.lumerical.com/ref_sim_obj_sources_tfsf.html`, Accessed: 2010-09-11.

(S3) Lumerical: advanced spatial absorption. `https://kb.lumerical.com/layout_analysis_pabs_adv.html`, Accessed: 2010-08-16.

(S4) Lumerical: Material Database. `https://kb.lumerical.com/materials_material_database_optical.html`, Accessed: 2010-09-11.

(S5) Palik, E. D. *Handbook of optical constants of solids*; Academic press, 1998; Vol. 3.

(S6) Kedenburg, S.; Vieweg, M.; Gissibl, T.; Giessen, H. Linear refractive index and absorption measurements of nonlinear optical liquids in the visible and near-infrared spectral region. *Optical Materials Express* **2012**, *2*, 1588–1611.

(S7) van Aarle, W.; Palenstijn, W. J.; Beenhouwer, J. D.; Altantzis, T.; Bals, S.; Batenburg, K. J.; Sijbers, J. The ASTRA Toolbox: A platform for advanced algorithm development in electron tomography. *Ultramicroscopy* **2015**, *157*, 35 – 47.

(S8) Baffou, G.; Berto, P.; Bermúdez Ureña, E.; Quidant, R.; Monneret, S.; Polleux, J.; Rigneault, H. Photoinduced heating of nanoparticle arrays. *Acs Nano* **2013**, *7*, 6478–6488.